



Titanium Nitride Plasmonic Nanohole Arrays for CMOS-Compatible Integrated Refractive Index Sensing: Influence of Layer Thickness on Optical Properties

Sebastian Reiter¹ · Weijia Han¹ · Christian Mai² · Davide Spirito² · Josmy Jose² · Marvin Zöllner² · Oksana Fursenko² · Markus Andreas Schubert² · Ivo Stemmler³ · Christian Wenger² · Inga Anita Fischer¹

Received: 16 January 2023 / Accepted: 20 February 2023
© The Author(s) 2023

Abstract

The combination of nanohole arrays with photodetectors can be a strategy for the large-scale fabrication of miniaturized and cost-effective refractive index sensors on the Si platform. However, complementary metal–oxide–semiconductor (CMOS) fabrication processes place restrictions in particular on the material that can be used for the fabrication of the structures. Here, we focus on using the CMOS compatible transition metal nitride Titanium Nitride (TiN) for the fabrication of nanohole arrays (NHAs). We investigate the optical properties of TiN NHAs with different TiN thicknesses (50 nm, 100 nm, and 150 nm) fabricated using high-precision industrial processes for possible applications in integrated, plasmonic refractive index sensors. Reflectance measurements show pronounced Fano-shaped resonances, with resonance wavelengths between 950 and 1200 nm, that can be attributed to extraordinary optical transmission (EOT) through the NHAs. Using the measured material permittivity as an input, the measured spectra are reproduced by simulations with a large degree of accuracy: Simulated and measured resonance wavelengths deviate by less than 10 nm, with an average deviation of 4 nm observed at incidence angles of 30° and 40°. Our experimental results demonstrate that an increase in the thickness of the TiN layer from 50 to 150 nm leads to a sensitivity increase from 614.5 nm/RIU to 765.4 nm/RIU, which we attribute to a stronger coupling between individual LSPRs at the hole edges with spatially extended SPPs. Our results can be used to increase the performance of TiN NHAs for applications in on-chip plasmonic refractive index sensors.

Keywords Integrated refractive index sensing · Plasmonic nanohole array · Titanium Nitride · Sensitivity · FDTD

Introduction

Application areas for miniaturized, cost-efficient biochemical sensors that enable real-time substance monitoring range from diagnostics in food industry to personalized healthcare solutions [1–4]. Optical sensors are capable of achieving high sensitivities; they can be fabricated cost-efficiently and

with a high degree of miniaturization. Furthermore, these sensors have the potential to allow label-free and rapid detection in applications. Optical sensors based on plasmonic effects, i.e., the resonant excitation of free electrons in metallic structures by incident light, have been commercialized [5]. Such sensors are based either on propagating surface plasmon polaritons (SPP) at a metallic/dielectric interface or localized surface plasmon resonances (LSPR), i.e., nonpropagating electron oscillations in metallic nanoparticles. In both cases, changes in the resonance wavelength as a result of changes in the refractive index (RI) in the surrounding dielectric can be used for sensing. However, external instruments such as microscopes and spectrometers are typically required for readout. In recent years, progress has been made towards further miniaturization by combining plasmonic nanostructures with optoelectronic devices [6–9]. Here, one strategy consists of combining plasmonic structures with commercially available CMOS

✉ Sebastian Reiter
Sebastian.reiter@b-tu.de

¹ Experimentalphysik und Funktionale Materialien, Brandenburgische Technische Universität Cottbus-Senftenberg, Erich-Weinert-Straße 1, 03046 Cottbus, Germany

² IHP–Leibniz Institut für Innovative Mikroelektronik, Im Technologiepark 25, 15236 Frankfurt (Oder), Germany

³ PerkinElmer LAS (Germany) GmbH, Ferdinand-Porsche-Ring 17, 63110 Rodgau, Germany

sensors [9]—in this case, the fabrication processes for the plasmonic structures and the CMOS sensor are separated. In even more compact approaches, plasmonic structures such as gratings [6, 7] or nanodisks [8] are positioned directly on top of a Si metal–oxide–semiconductor (MOS) structure [7] or a Si photodiode [6, 8] in the same fabrication process, with potential for an even higher degree of miniaturization and the integration with signal-conditioning circuits on-chip. The integration of plasmonic nanohole arrays (NHAs), i.e., thin metallic layers perforated with arrays of subwavelength-sized holes, with Ge photodetectors in particular led to an integrated device that was highly sensitive to permittivity changes in the vicinity of the device [10]. In plasmonic NHAs, extraordinary optical transmission (EOT) of light can be observed as narrow, Fano-shaped resonances in transmission spectra [11]. The asymmetric Fano shape results from the coupling of an excitation with a narrow line shape, such as SPPs and Rayleigh anomalies (RA), originating from the diffraction of light parallel to the NHA surface, with a broad background. The optical properties of the resonance are highly sensitive to changes in the dielectric environment, and changes in the RI of the surrounding dielectric can be detected via a shift of the resonance peak. When the NHA is combined with a photodetector, this peak shift is directly converted to a change in photocurrent under illumination with monochromatic incident light. This can be used to detect changes in the RI of the surrounding dielectric in an on-chip RI sensor, which also enables a straightforward cointegration with electronic read-out circuits.

For plasmonic applications, the noble metals Au and Ag are most widely used since they exhibit comparatively low losses at visible and NIR wavelengths [12]. However, those metals are incompatible with complementary metal–oxide–semiconductor (CMOS) technology, which is a prerequisite for the cost-effective on-chip fabrication of plasmonic structures combined with optoelectronic devices. Among the CMOS-compatible metals that can be used, the transition metal nitride Titanium Nitride (TiN) is highly interesting [13]. TiN has been investigated previously for plasmonic applications [14–16]; it is biocompatible as well as chemically stable and, in contrast to Au and Ag, associated with low fabrication cost as well as high thermal stability. Moreover, TiN is a well-established material and compatible to CMOS technology. However, since the imaginary part of the permittivity of TiN is large, the large optical losses compared to e.g. Au and Ag at visible and NIR wavelengths can be expected to have a negative impact on optical properties and it is important to identify parameters that can be utilized to tune the performance of plasmonic structures made from TiN for sensing.

In the present work, TiN NHAs with square array configurations and different thicknesses of the TiN were fabricated in an industrial processing line [17]. We present results of

structural and optical characterization and discuss those in the context of TiN layer thickness. We compare measured reflectance spectra to finite-difference time-domain (FDTD) simulation results based on the measured permittivities of the fabricated TiN films in both air and acetone. Our results show that the thickness of the TiN layer not only affects the spectral shape of EOT in our NHAs but also has an impact on the resonance shifts observed as a result of changes in the superstrate RI, which becomes more pronounced as the TiN layer thickness increases. This work, therefore, provides valuable insights for the use of TiN as NHA material for on-chip RI sensors fabricated using CMOS technology.

Methods

Sample fabrication was carried out in an industrial 8" processing line [17]. For all samples, p-doped (100) Silicon (Si) wafers with dopant concentrations $N_A = 10^{15} \text{ cm}^{-3}$ served as substrates. A SiO_2 layer with a target thickness of 200 nm was deposited using a plasma-enhanced chemical vapor deposition (PECVD) process with tetraethyl orthosilicate (TEOS) as a precursor on top of the Si substrate. As a next step, thin TiN films were deposited by sputtering with thicknesses of 50 nm (sample A), 100 nm (sample B), and 150 nm (sample C). The NHAs with sizes of $3 \times 3 \text{ mm}^2$ in the TiN layer were structured via deep ultraviolet (DUV) photolithography and reactive ion etching (RIE). Figure 1a shows a schematic drawing of the TiN NHA on SiO_2 and Si substrate.

The analysis of the crystalline orientation and the thickness of the sputtered TiN films was carried out via grazing incidence (GI) and specular X-ray diffraction (XRD) as well as X-ray reflectivity (XRR), respectively. XRR measurements are simulated by RCRRefSimW software

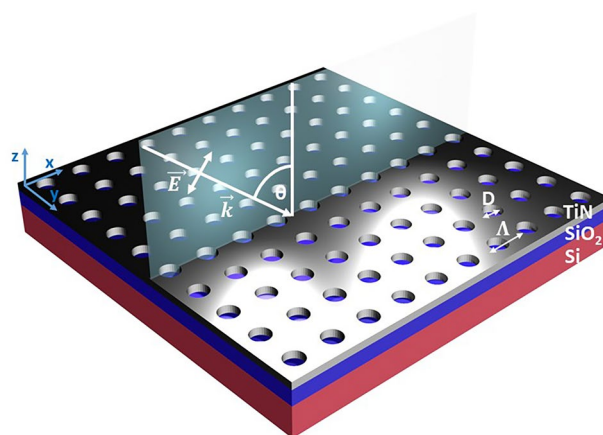


Fig. 1 Schematic drawing of a fabricated TiN NHA on a layered substrate consisting of SiO_2 and Si

exploiting dynamical theory of X-ray reflection using the matrix approach. The material permittivity was measured by spectroscopic ellipsometry for wavelengths between 250 and 1600 nm. Atomic force microscopy (AFM) was used for the characterization of the surface roughness. The geometries of the fabricated NHAs were investigated using both SEM and transmission electron microscopy (TEM). Optical characterization of the NHA was carried out by measuring reflectance spectra with a spectrometer (PerkinElmer LAMBDA 1050 + UV/Vis/NIR with total absolute measurement system (TAMS) module) at different incident angles for wavelengths between 800 and 1600 nm at room temperature.

Simulated reflectance spectra were obtained using the commercial FDTD solver Lumerical [18]. While other numerical approaches can be used (such as e.g. the Finite-Element-Method (FEM) [19], the Finite-Difference-Frequency-Method (FDFD) [20], or the Method-of-Moments (MoM) [21]), FDTD simulations have the advantage that the approach is particularly well adapted to solving Maxwell's equations [22] and, thus, generally robust [23]. As a result, FDTD approaches are widely applied to the simulation of plasmonic structures [19]. For the simulation of our structures, we chose the following settings: nonperpendicular incidence of light was realized by setting the plane wave source to type broadband fixed angle source technique (BFAST) [24]. The perfectly matched layers (PML) as boundary conditions in the z-direction were realized using the profile *steep angle* with 16 layers. The Yee-Cells had a maximum mesh step of 6 nm in every direction.

Results and Discussion

Material and Structural Characterization

While the optical properties of TiN NHAs are primarily determined by the material permittivity, the morphology of the NHAs, in particular the roughness of the plasmonic layer, can also have an impact on optical properties and lead to, e.g., broadening of resonances [25, 26]. Deposition by sputtering can e.g. lead to higher surface roughness than alternative deposition methods. Therefore, we also present and discuss characterization results pertaining to the crystallinity and surface roughness of our TiN films obtained from GIXRD, XRD, XRR, and AFM measurements.

In the GIXRD spectrum obtained from sample B, three representative peaks at 36.6°, 42.6°, and 61.7° can be attributed to the (111), (200), and (220) orientations of the fcc TiN phase (JCPDS 00–038–1420), indicating polycrystalline quality of the TiN film (Fig. 2a). The peak at 55.6° is related to the Si substrate. Specular XRD in Fig. 2b reveals that the planes parallel to the surface are dominated by three

characteristic peaks at 33.0°, 36.6°, and 69.2° pertaining to Si (002) (due to “*Umweganregung*”), TiN (111), and Si (004) orientation. This confirms that the (111) orientation dominates in TiN growth, as also illustrated by GIXRD spectrum where the strongest peak originates from the (111) plane, which is caused by the lowest strain energy of the prepared TiN film [27]. The XRR pattern (red line) accompanied by the fitting curve (green line) in Fig. 2c gives further insights into the properties of TiN film. Fitted parameters (inset table) reflect the estimated film thickness of ~102.1 nm and 208.5 nm for TiN and SiO₂. These are in good agreement with the thicknesses targeted in sample B fabrication. The average surface roughness is ~2.13 nm for TiN and ~0.58 nm for the TiN/SiO₂ interface, which indicates a relatively smooth surface of the TiN film and that the deposited SiO₂ layer remains intact during sputtering.

The surface roughness is an important parameter to determine the quality of the NHAs. The AFM images in Fig. 3 show the morphology of TiN surfaces for samples A (a), B (b), and C (c). The AFM measurements were taken at the center of the wafer at a 10 × 10 μm² area. Table 1 shows the root mean square (rms) surface roughness for these TiN films. The surface roughness of the TiN layers increases with increasing thickness. However, the maximum measured roughness shows an rms value of 1.277 nm, which indicates a low surface roughness of all fabricated films. Our simulations show no difference in the optical properties of the NHA fabricated from ideally smooth films compared to films with the measured roughness. Compared to the XRR measured roughness, the AFM measured roughness for sample B is significantly lower. This difference can be explained by the larger area that is covered by X-ray beam compared the AFM measurements [28].

The complex permittivities of the sputtered TiN films (Fig. 4a, b) were determined by spectroscopic ellipsometry. Previous investigations have shown that the deposition method as well as deposition parameters can have a large influence on the optical properties of TiN films [29]. Indeed, a slight variation in the wavelength dependence of the permittivity can even be observed for the TiN films of different thicknesses. For the TiN films with a thickness of 50 nm (black line), the real part of the permittivity (ϵ'_{TiN}) becomes negative for wavelengths > 613 nm. For a thickness of 100 nm (red line) and 150 nm (blue line), this crossover point shifts to slightly larger wavelengths (626 nm and 649 nm, respectively). For larger wavelengths, the material becomes metallic and can e.g. support SPPs. The imaginary part of the permittivity (ϵ''_{TiN}) is related to material damping. For the sputtered TiN films, a higher thickness is associated with a smaller (ϵ''_{TiN}) (Fig. 4b).

The complex permittivities for all three thicknesses can be represented by a Lorentz-Drude model [31]

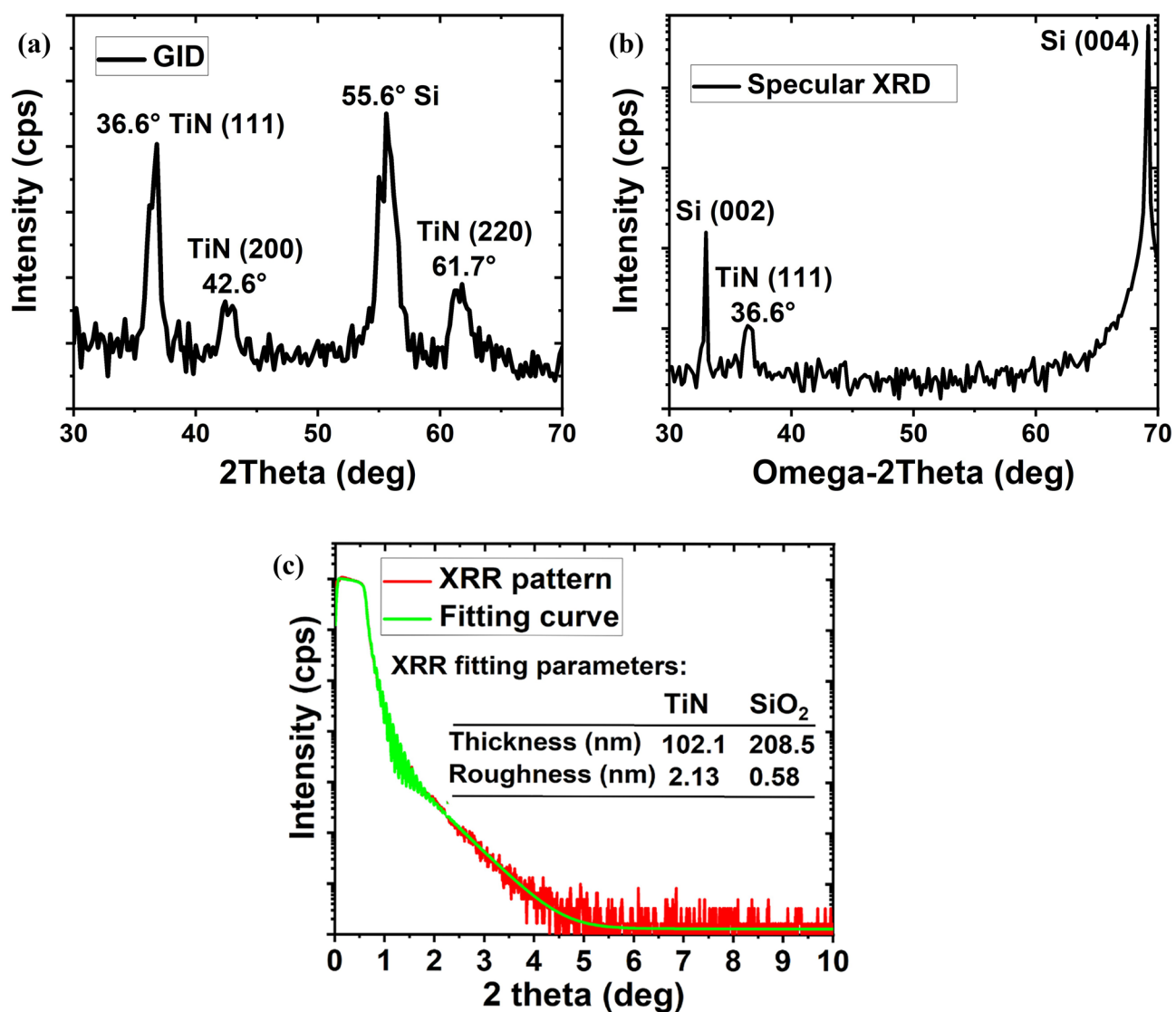


Fig. 2 Grazing incidence X-ray diffraction (GIXRD) spectrum (a), specular X-ray diffraction (XRD) pattern (b), and X-ray reflectivity (XRR) curve (c) obtained from sample B

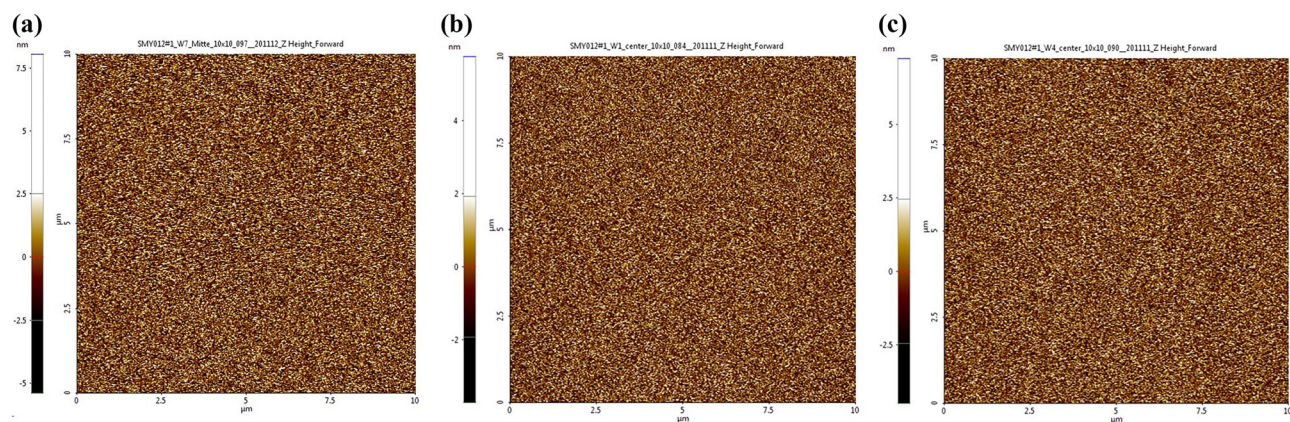


Fig. 3 AFM images showing surface morphologies of sample A (a), sample B (b), and sample C (c)

Table 1 rms surface roughness of deposited TiN films in different thicknesses

Sample	rms surface roughness (nm)
A (50 nm TiN)	0.985
B (100 nm TiN)	1.255
C (150 nm TiN)	1.277

$$\epsilon(E) = \epsilon_\infty + \frac{E_{pl}^2}{-E^2 - iE\Gamma_D} + \sum_j \frac{f_i E_{pl}^2}{E_j^2 - E^2 - iE\Gamma_j}, \quad (1)$$

where ϵ_∞ is the high-frequency dielectric constant, E_{pl} is the plasma energy, Γ_D is the damping factor in the Drude model, f_i is the oscillator strength in the Lorentz model, E_j is the energy, and Γ_j is the damping factor of the j -th Lorentz

oscillator and i is the imaginary unit. All permittivities can be fit using one Drude component and three Lorentz oscillators (see Fig. 4c for an example fit), and the fit parameters for the different thicknesses are reported in Table 2.

Even though the TiN sputtering process used here was not specifically tuned for optimum optical properties, the optical properties of our films compare well to other results, where TiN was deposited using atomic layer deposition (ALD) [30] (dashed green lines in Fig. 4a and b. The ALD deposited layer has a larger (ϵ''_{TiN}) between 250 nm and around 470 nm. For wavelengths > 470 nm, the damping of the sputtered TiN is slightly higher. This changes again for larger wavelengths > 1050 nm. After that point, the damping for the sputtered TiN films is lower than that for the ALD material. Our characterization results indicate that the sputtered TiN films exhibit optical properties that are comparable to results

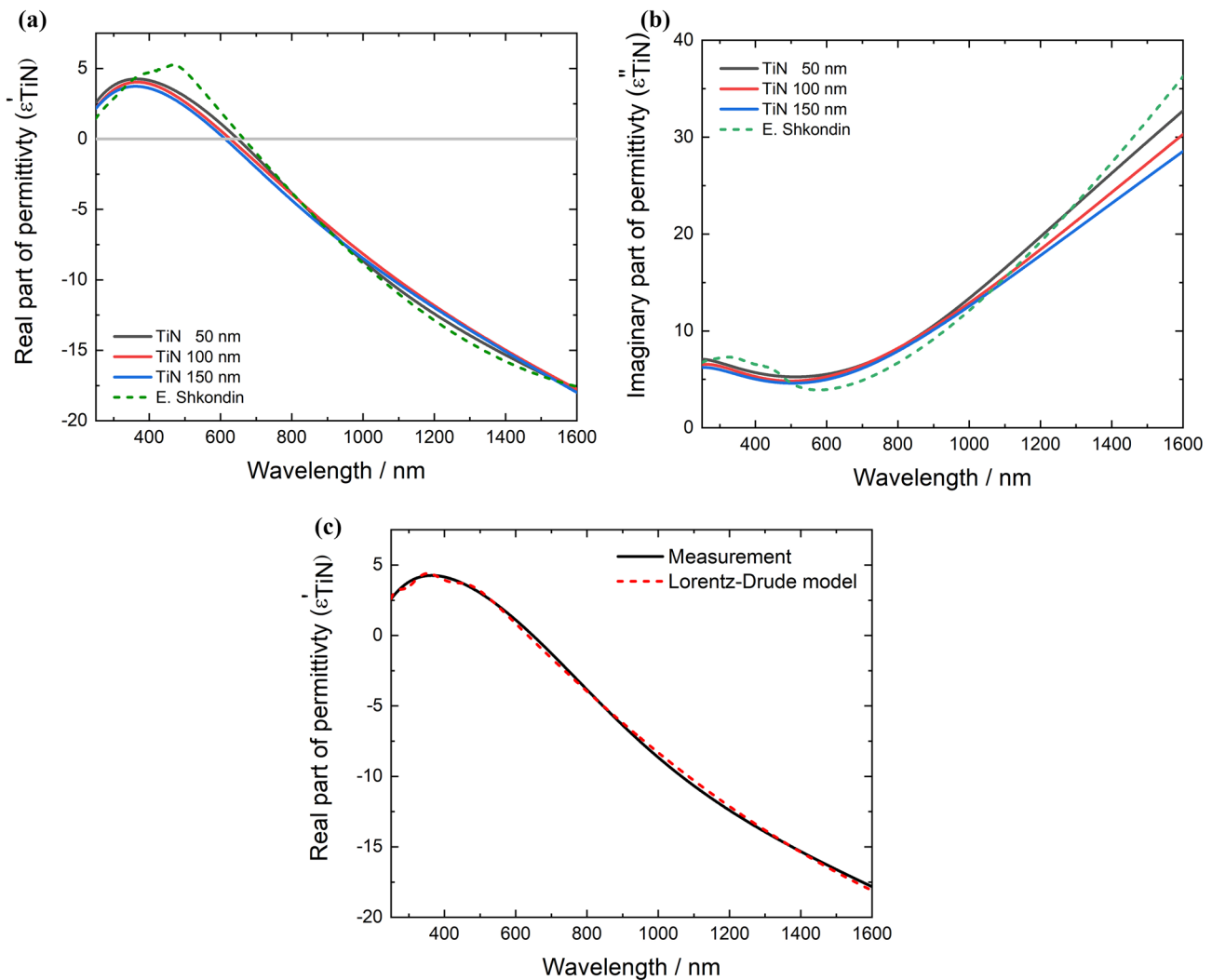


Fig. 4 Real part (a) and imaginary part (b) of the permittivities of sputtered TiN films with different thickness (solid lines) compared to ALD-grown TiN (dashed lines) [30]. Comparison of measured real

part of the permittivity with the Lorentz-Drude-model-based fit for sample A (50 nm TiN) (c)

Table 2 Parameter values describing the complex permittivities $\epsilon(E)$ for samples A, B, and C at wavelengths ranging from 250 to 1600 nm

	Sample A (50 nm)	Sample B (100 nm)	Sample C (150 nm)
ϵ_∞ (eV)	2.7179	0.7839	0.1902
E_{pl} (eV)	6.3656	6.0808	5.9560
Γ_D (eV)	0.9896	0.9426	0.9309
E_1 (eV)	2.8378	2.9655	2.9107
f_1 (eV)	0.1312	0.0469	0.0319
Γ_1 (eV)	1.0486	0.9934	0.8013
E_2 (eV)	3.9394	4.0000	3.9031
f_2 (eV)	0.5738	0.4458	0.4406
Γ_2 (eV)	1.6528	2.0000	2.0000
E_3 (eV)	5.4556	6.6355	6.5508
f_3 (eV)	1.8662	6.0000	6.0000
Γ_3 (eV)	1.9726	5.1801	4.5697

obtained from ALD-grown films. For a RI sensor with a Ge photodiode the behavior of the NHA in the wavelength range of 1200–1600 nm is the most interesting. In this range, the sputtered TiN films show lower damping than the ALD-grown films. Sputter processes are much faster and cheaper than ALD growth. The fabrication speed and costs are very relevant factors for the envisaged use as an integrated part of a RI sensor.

Finally, SEM and TEM images were used to characterize the quality of the NHA geometries after fabrication. Figure 5a shows the top view of the fabricated NHA with a pitch of $\Lambda = 800$ nm and a hole diameter of $D = 600$ nm. The dimensional lines drawn into the image show that the geometry of the NHA has been fabricated with a very high accuracy. It can also be seen that the holes are well defined and of very uniform dimensions. This homogeneity extends over the whole 3×3 mm² area, showing the advantage of

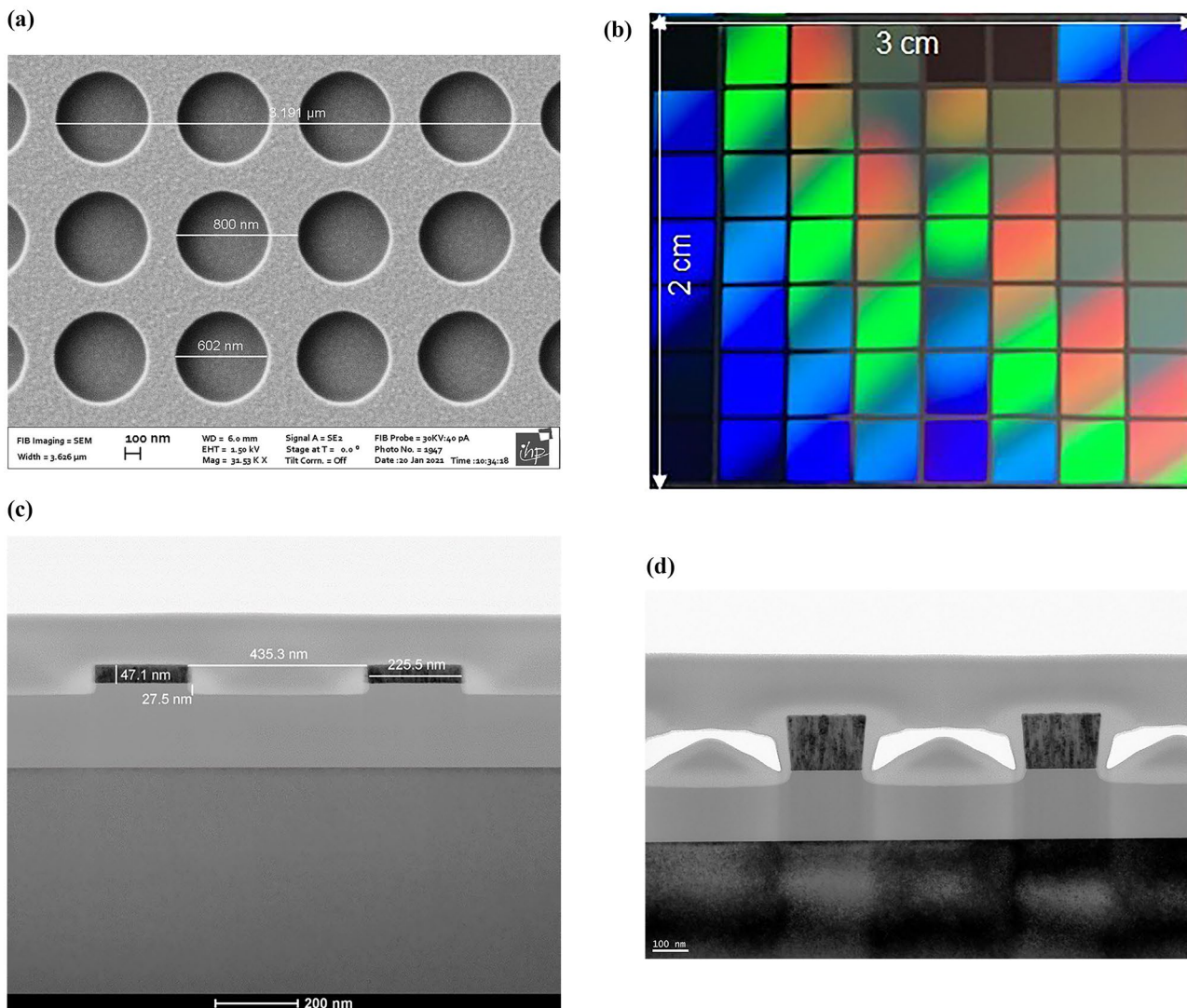


Fig. 5 a SEM image of a sputtered TiN NHA with a pitch of $\Lambda = 800$ nm and a hole diameter of $D = 600$ nm. b Wafer with 3×3 mm NHAs with different pitches and hole diameters. Cross-sectional TEM images of c sample A and d sample B

using industrial lithography processes for the fabrication of these plasmonic structures. The cross-section in Fig. 5c, d indicates clear and sharp delimitations of the individual material layers. The edges of the etched TiN layer incline slightly inwards but are still steep. The SiO₂ layer was etched ~ 30 nm deep by RIE during the structuring process. The TiN layer thickness of sample A in Fig. 5c is ~ 3 nm thinner than the target thickness. A photographic image of a chip of TiN NHAs in Fig. 5b shows color transitions that result from the different NHA geometries of each square on the sample.

Optical Characterization of Plasmonic Nanohole Arrays

The enhanced transmission through a NHA for a certain resonance wavelength has been explained by the excitation of SPP by light on the incident surface, transmission through the hole to the opposite site of the metallic film, and reemission of photons [32]. In a 2D square array (Fig. 1a), the excitation of SPP by incident light can only occur if the momentum matching condition $\mathbf{k}_{SPP} = \mathbf{k}_0 \sin \theta \pm n\mathbf{G}_x \pm m\mathbf{G}_y$ is fulfilled [24, 25]; this condition can be used to derive the corresponding excitation wavelength λ_{SPP} . Here, \mathbf{k}_{SPP} is the wave vector of the SPP.

$$|\mathbf{k}_{SPP}| \equiv k_{SPP} = Re \left(\frac{\omega}{c} \sqrt{\frac{\epsilon_{TiN} + \epsilon_D}{\epsilon_{TiN}\epsilon_D}} \right), \tag{2}$$

where \mathbf{k}_0 is the wave vector of incident light with incidence angle θ (Fig. 1a), (n, m) are integers denoting the respective SPP modes, and $\mathbf{G}_x, \mathbf{G}_y = 2\pi/\Lambda$ are the reciprocal lattice constants of the grating with pitch Λ . Furthermore, ω is the angular frequency, c is the speed of light in vacuum, and $\epsilon_{TiN}, \epsilon_D$ are the permittivities of the TiN and the dielectric, respectively. In addition to SPPs at the TiN-dielectric interfaces and LSPRs excited at the holes, Rayleigh anomalies (RA) resulting from light diffraction parallel to the grating surface have also been shown to play a role in influencing the optical properties of NHAs [34]. Their wave vector \mathbf{k}_{RA} fulfills a similar momentum matching condition as \mathbf{k}_{SPP} , with

$$|\mathbf{k}_{RA}| = \frac{\omega}{c} \sqrt{\epsilon_D} \tag{3}$$

In contrast to SPPs, RAs do not depend on the material properties of the grating but only on its geometry and the permittivity of the dielectric environment.

While an application of the fabricated NHAs to on-chip sensing mostly relies on the transmittance properties of the NHA, we focus on measurements of the reflectance spectra here instead. The relationship between transmittance (T) and reflectance

(R) and losses (L) resulting from absorption and scattering is $R = 1 - T - L$. Compared to the transmittance, the measurement of the reflectance has the advantage that the absorption in the Si substrate does not have to be considered for the evaluation and, thus, contributes no additional source of error.

Figure 6a–c shows the measured reflectance spectra of fabricated NHAs for samples A (50 nm TiN), B (100 nm TiN), and C (150 nm TiN) for different incidence angles of light using p-polarized light. EOT can be clearly recognized as the first-order Fano resonances in the spectra with characteristic asymmetric resonance shapes. With increasing incidence angles θ (Fig. 1a), the reflectance dips, which are associated with transmission peaks, exhibit red shifts (see Eq. (2)) and reduced peak widths. Compared to the simulated spectra (dashed lines), the measured reflectance spectra show lower intensities especially for higher angles of incidence, possibly related to some signal intensity loss in the measurement setup as a result of surface roughness or sample alignment. The positions of the dips match very well between simulation and experiment, which validates the simulation approach and attests to the large-scale homogeneity of the NHAs. The calculated $(+1, 0)$ SPP and $(+1, 0)$ RA excitation wavelengths are inserted as vertical dashed and dotted lines in the spectra. We note that these lines can be seen to align with the peaks situated at slightly lower wavelengths than the Fano dips [35]. The linewidth of the Fano-shapes is broad for small incident angles of light and becomes narrower for higher angles of incidence. An increased incidence angle can both enhance the interaction of different resonant modes [36] and improve the collection of scattered optical energy from one hole by its neighboring holes [37], leading to a decrease in radiative losses. Both effects contribute to a narrowing of the linewidth.

The Fano resonances become more pronounced with increasing TiN thickness. This can be clearly seen in Table 3, which shows the EOT visibility (defined as the difference between maximum and minimum reflectance divided by the average one [38]) of the simulated and measured spectra for an incidence angle of 40° for p-polarized light.

It can clearly be seen that the EOT visibility for sample A is significantly lower compared to that for sample B and C. Indeed, the SPP penetration depth in TiN (approx. 50 nm for incident light with a wavelength of 1200 nm) is slightly larger than the TiN thickness for sample A, leading to a reduced EOT visibility for the NHA in the optically thin film of sample A.

Figure 6d–f shows the reflectance spectra for s-polarized light for samples A, B, and C. Owing to the relative orientation of the E -field vector and high symmetry directions of the lattice, the influence of the angle of incidence on the wavelength-dependence on the reflectance is strongly reduced compared to p-polarized light [33].

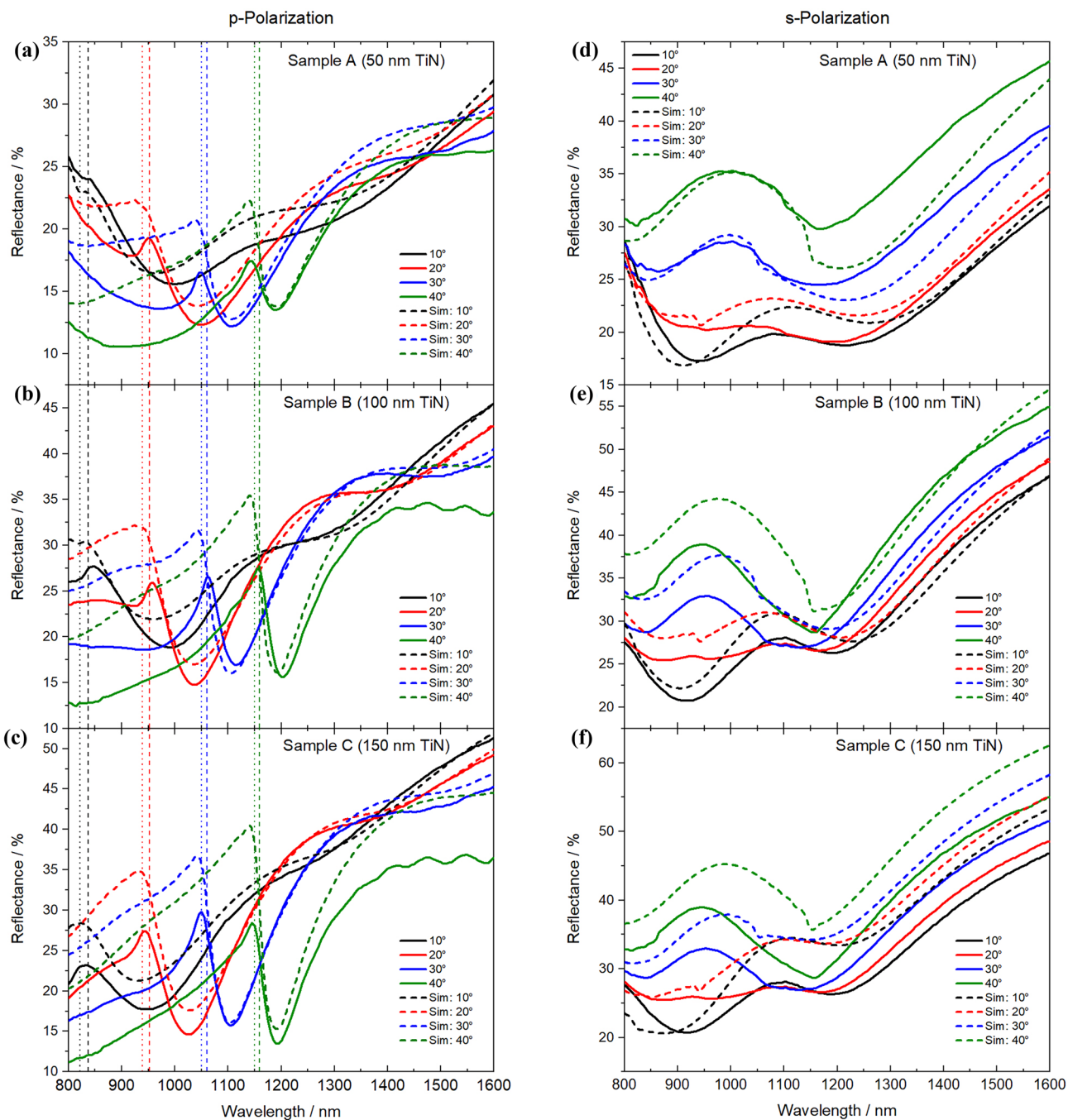


Fig. 6 Measured and simulated reflectance spectra of samples A, B, and C under different angles of incidence and with **a–c** p-polarized as well as **d–f** s-polarized light. Dashed spectral lines show simulated

spectra. Vertical lines indicate analytical results for the positions of the SPP resonances (dashed lines) and the RAs (dotted lines)

Finally, we investigate the influence of the TiN layer thickness on sensing performance. A commonly used parameter to quantify the resonance shift due to a change in the RI is the sensitivity S defined as $S = \frac{\Delta\lambda_{Res}}{\Delta n}$, where $\Delta\lambda_{Res}$ corresponds to resonance shift and Δn is the change of the RI of the surrounding dielectric. The measurement

of the bulk sensitivity was carried out by measuring reflectance spectra in air and in acetone. For measurements in liquid, the samples were submerged in a cylindrical beaker filled with acetone, which was placed in the middle of the sample chamber. The baseline was measured in transmission. The strong absorption in acetone at wavelengths

Table 3 Measured and simulated EOT visibility as a function of TiN thickness for an incidence angle of 40° and p-polarized light

Sample	Simulated EOT visibility	Measured EOT visibility
A (50 nm TiN)	0.47	0.25
B (100 nm TiN)	0.75	0.55
C (150 nm TiN)	0.9	0.71

between 1130 and 1210 nm as well as 1335 and 1500 nm (Fig. 7c) limits the angle of incidence, which has to be chosen in such a way that the reflectance dips are not positioned within these wavelength ranges. Figure 7a, b show the measured (solid lines) and simulated (dashed lines) spectra for an incidence angle of 15° and p-polarized light. Wavelength ranges, where absorption in acetone is large, are shaded in gray. Simulated and measured reflectance dips show good agreement. Table 4 shows the simulated and measured sensitivities.

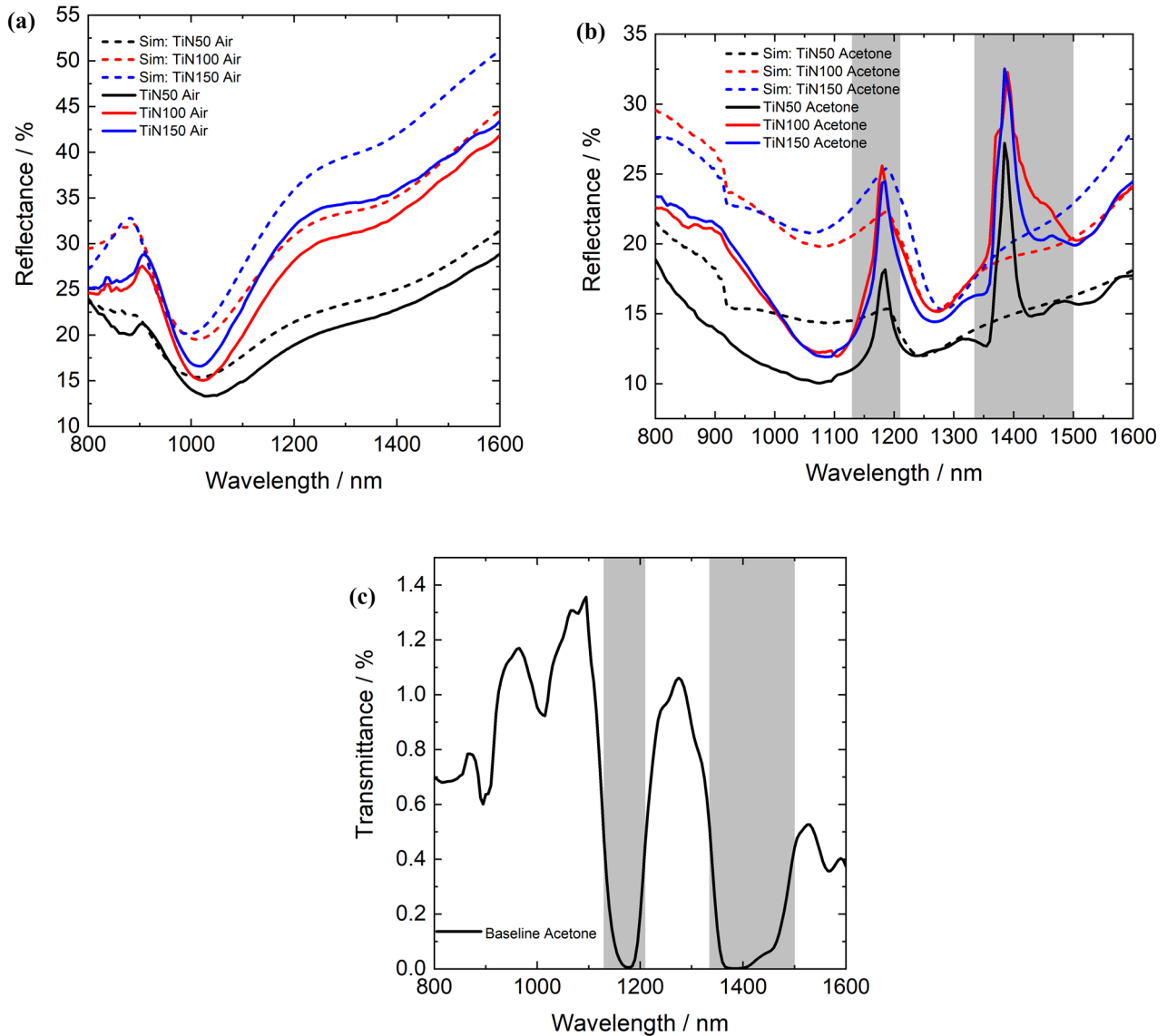


Fig. 7 Reflectance measurements in air (a) and acetone (b) for the calculation of sensitivities with an incidence angle of 15° and using p-polarized light. The transmittance baseline of the measurements in acetone (c) shows strong absorption in two wavelength ranges highlighted in gray

Table 4 Simulated and measured sensitivities of NHAs with different thicknesses of TiN layers

Sample	Simulated sensitivity (nm/RIU)	Measured sensitivity (nm/RIU)
A (50 nm TiN)	665.5	614.5
B (100 nm TiN)	715.1	720.7
C (150 nm TiN)	804.5	765.4

The measurement results confirm the trend of the simulation, which shows an increasing sensitivity with increasing TiN thickness. Figure 8 shows the simulated E_z distribution of the NHA in a x - z plane cross-section for p-polarized light with an incidence angle of 40° and a wavelength of $\lambda = 1200\text{nm}$, which corresponds to the Fano-resonance wavelength (Fig. 6a–c). We observe strong near field enhancement at the edges of the TiN film. Importantly, an

increase both in spatial extent of the region with enhanced field amplitude and in peak amplitude of the E-field can be observed for thicker TiN layers when comparing samples A, B and C (Fig. 8a–c). We attribute this to a stronger coupling between individual LSPRs at the hole edges with spatially extended SPPs, which can be an explanation for the increase in sensitivity of the NHA with increasing film thickness.

Finally, a comparison of our measured sensitivities with simulated sensitivities for different realizations of TiN-based refractive index sensors is reported in Table 5. While higher sensitivities are predicted for some approaches and, indeed, other approaches using the metals Ag and Au for plasmonic refractive index sensing [39–42], compared to our approach; our TiN NHAs have the advantage of being fabricated with relative ease and straightforward integration with device fabrication [10]. Nonetheless, the comparison also shows the potential for utilizing structures other than nanohole arrays for refractive index sensing.

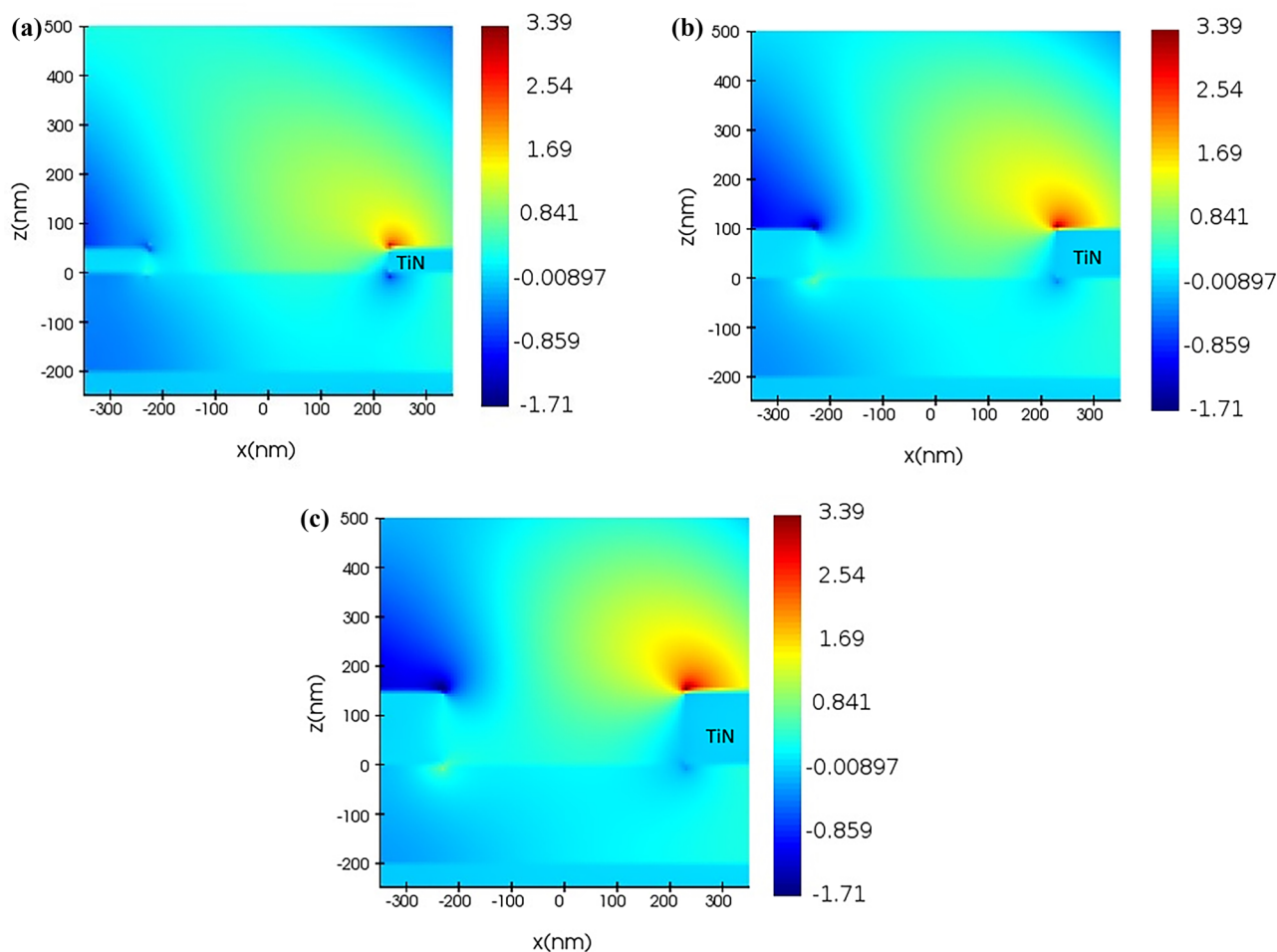
**Fig. 8** Cross-sectional plots of simulation results for the E_z distribution of samples A (a), B (b), and C (c) obtained under illumination with p-polarized light at a wavelength of 1200 nm and at 40° incidence angle

Table 5 Measured and calculated sensitivities for plasmonic sensing concepts based on TiN

Reference	Sensing structure	Experiment/simulation	Sensitivity (nm/RIU)
[43]	Straight waveguide coupled with groove and square ring resonator in TiN film	Simulation	1074.88
[44]	Photonic crystal fiber coated with TiN	Simulation	~ 10,000
[45]	TiN nanosphere multimers	Simulation	~ 140
this work	TiN nanohole array	Experiment	765.4

Conclusion

TiN is a CMOS compatible and biocompatible transition metal nitride with large thermal stability, which could make it interesting for applications in on-chip sensing. The large optical losses in TiN with their potentially negative impact on sensing performance motivate our investigation of parameters that can be used to boost properties for sensing applications. Here, we investigated the influence of metallic layer thickness on the optical properties of TiN NHAs. To this end, thin, sputtered TiN films with three different thicknesses 50, 100, and 150 nm were fabricated in an industrial production line. Our material and structural characterization results show that films with good crystallinity and low surface roughness were fabricated, whose material permittivities are comparable to literature results for films deposited by ALD. Furthermore, the fabrication process based on DUV lithography and dry etching yielded excellent homogeneity over the full $3 \times 3 \text{ mm}^2$ area of the NHAs. Our optical characterization of the fabricated structures based on reflectance spectra shows the appearance of Fano resonances at specific wavelengths related to the array geometry as well as the superstrate RI. The Fano resonances become more pronounced at increasing angle of incidence as well as increasing TiN layer thickness. Most importantly, both measurements in air and acetone as well as simulations show that increasing the TiN layer thickness significantly boosts sensitivities with respect to superstrate RI changes.

Our results show that the TiN layer thickness is a parameter that has a strong positive impact on the performance of TiN NHAs for sensing applications. Our investigation, thus, provides valuable insights for the use of TiN NHAs in CMOS compatible, on-chip RI sensors, where improved performance can be achieved using TiN thicknesses of 150 nm.

Author Contribution Simulation, spectrometric measurements, data analysis, and manuscript preparation were performed by Sebastian Reiter. Data analysis and spectrometric measurements were performed by Weijia Han. Device development and fabrication were performed by Christian Mai. Device design and characterization were performed by Davide Spirito. Development of fabrication processes was performed by Josmy Jose. XRD characterization was performed by Marvin Zöllner. AFM characterization were performed by Oksana Fursenko. TEM measurements was performed by Markus Andreas Schubert. Spectrometric measurements were performed by Ivo Stemmler.

Conceptualization was performed by Christian Wenger. Conceptualization, data analysis, and manuscript preparation were performed by Inga Fischer.

Funding Open Access funding enabled and organized by Projekt DEAL. This work was supported by Bundesministerium für Bildung und Forschung (Grant numbers: 16ES1128K, 16ME0420K and 16ES1131, 16ME0424). This work was supported by HLRN–Norddeutscher Verbund für Hoch- und Höchstleistungsrechner (Account: bbp00044).

Data Availability The simulation results come from Ansys Lumerical FDTD simulations using the Lumerical material library or measured material data. Calculations were performed using the theoretical formulas and the software Matlab using measured material data or material data from Lumerical material library. The measured data are available from the corresponding author on reasonable request.

Declarations

Ethics approval Not applicable. This manuscript does not contain experiments on ethical issue.

Consent to participate Not applicable.

Consent for publication Not applicable.

Competing interests The authors have no relevant financial or non-financial interests to disclose.

Open Access This article is licensed under a Creative Commons Attribution 4.0 International License, which permits use, sharing, adaptation, distribution and reproduction in any medium or format, as long as you give appropriate credit to the original author(s) and the source, provide a link to the Creative Commons licence, and indicate if changes were made. The images or other third party material in this article are included in the article's Creative Commons licence, unless indicated otherwise in a credit line to the material. If material is not included in the article's Creative Commons licence and your intended use is not permitted by statutory regulation or exceeds the permitted use, you will need to obtain permission directly from the copyright holder. To view a copy of this licence, visit <http://creativecommons.org/licenses/by/4.0/>.

References

- Hill RT (2015) Plasmonic biosensors. *WIREs Nanomed Nanobiotechnol* 7(2):152–168. <https://doi.org/10.1002/wnan.1314>
- Balbinot S, Srivastav AM, Vidic J, Abdulhalim I, Manzano M (2021) Plasmonic biosensors for food control. *Trends Food Sci Technol* 111:128–140. <https://doi.org/10.1016/j.tifs.2021.02.057>

3. Song L, Chen J, Xu BB, Huang Y (2021) Flexible plasmonic biosensors for healthcare monitoring: progress and prospects. *ACS Nano*. <https://doi.org/10.1021/acsnano.1c07176>
4. Brolo AG (2012) Plasmonics for future biosensors. *Nat Photon* 6(11):709–713. <https://doi.org/10.1038/nphoton.2012.266>
5. Owen V (1997) Real-time optical immunosensors — a commercial reality. *Biosens Bioelectron* 12(1):i–ii. [https://doi.org/10.1016/0956-5663\(96\)89090-7](https://doi.org/10.1016/0956-5663(96)89090-7)
6. Ajiki Y, Kan T, Matsumoto K, Shimoyama I (2018) Electrically detectable surface plasmon resonance sensor by combining a gold grating and a silicon photodiode. *Appl Phys Express* 11(2):022001. <https://doi.org/10.7567/APEX.11.022001>
7. Patskovsky S, Meunier M (2013) Integrated Si-based nanoplasmonic sensor with phase-sensitive angular interrogation. *Ann Phys* 525(6):431–436. <https://doi.org/10.1002/andp.201300078>
8. Mazzotta F, Wang G, Hägglund C, Höök F, Jonsson MP (2010) Nanoplasmonic biosensing with on-chip electrical detection. *Biosens Bioelectron* 26(4):1131–1136. <https://doi.org/10.1016/j.bios.2010.07.008>
9. Tokel O, Yildiz UH, Inci F, Durmus NG, Ekiz OO, Turker B, Cetin C, Rao S, Sridhar K, Natarajan N, Shafiee H, Dana A, Demirci U (2015) Portable microfluidic integrated plasmonic platform for pathogen detection. *Sci Rep* 5(1):9152. <https://doi.org/10.1038/srep09152>
10. Augel L, Kawaguchi Y, Bechler S, Körner R, Schulze J, Uchida H, Fischer IA (2018) Integrated collinear refractive index sensor with Ge PIN photodiodes. *ACS Photonics* 5(11):4586–4593. <https://doi.org/10.1021/acsp Photonics.8b01067>
11. Ebbesen TW, Lezec HJ, Ghaemi HF, Thio T, Wolff PA (1998) Extraordinary optical transmission through sub-wavelength hole arrays. *Nature* 391(6668):667–669. <https://doi.org/10.1038/35570>
12. West PR, Ishii S, Naik GV, Emani NK, Shalae VM, Boltasseva A (2010) Searching for better plasmonic materials. *Laser Photonics Rev* 4(6):795–808 (2010). <https://doi.org/10.1002/lpor.200900055>
13. Stockman MI, Kneipp K, Bozhevolnyi SI, Saha S, Dutta A, Ndukaife J, Kinsey N, Reddy H, Guler U, Shalae VM, Boltasseva A, Gholipour B, Krishnamoorthy HNS, MacDonald KF, Soci C, Zheludev NI, Savinov V, Singh R, Groß P, Lienau C, Vadai M, Solomon ML, Barton DR, Lawrence M, Dionne JA, Boriskina SV, Esteban R, Aizpurua J, Zhang X, Yang S, Wang D, Wang W, Odom TW, Accanto N, de Roque PM, Hancu IM, Piatkowski L, van Hulst NF, Kling MF (2018) Roadmap on plasmonics. *J Opt* 20(4):043001. <https://doi.org/10.1088/2040-8986/aaa114>
14. Chang C-C, Nogan J, Yang Z-P, Kort-Kamp WJM, Ross W, Luk TS, Dalvit DAR, Azad AK, Chen H-T (2019) Highly plasmonic titanium nitride by room-temperature sputtering. *Sci Rep* 9(1):15287. <https://doi.org/10.1038/s41598-019-51236-3>
15. Naik GV, Schroeder JL, Ni X, Kildishev AV, Sands TD, Boltasseva A (2012) Titanium nitride as a plasmonic material for visible and near-infrared wavelengths. *Opt Mater Express* 2(4):478. <https://doi.org/10.1364/OME.2.000478>
16. Guo W-P, Mishra R, Cheng C-W, Wu B-H, Chen L-J, Lin M-T, Gwo S (2019) Titanium nitride epitaxial films as a plasmonic material platform: alternative to gold. *ACS Photonics* 6(8):1848–1854. <https://doi.org/10.1021/acsp Photonics.9b00617>
17. Mai C, Marschmeyer S, Peczek A, Kroh A, Jose J, Reiter S, Fischer I, Wenger C, Mai A (2022) Integration aspects of plasmonic TiN-based nano-hole-arrays on Ge photodetectors in a 200mm wafer CMOS compatible silicon technology. *ECS Meeting Abstracts MA2022–02*, 1174–1174. <https://doi.org/10.1149/10904.0035ecst>
18. Lumerical Inc. FDTD: 3D electromagnetic simulator (n.d.) <https://www.ansys.com/products/Photonics/fdtd>. Accessed 23 December 2022
19. Gray SK (2013) Theory and modeling of plasmonic structures. *J Phys Chem C* 117(5):1983–1994. <https://doi.org/10.1021/jp309664c>
20. Veronis G, Fan S (2007) Overview of simulation techniques for plasmonic devices," in *Surface Plasmon Nanophotonics*, M. L. Brongersma and P. G. Kik, eds., Springer Series in Optical Sciences (Springer Netherlands, 2007), pp. 169–182. https://doi.org/10.1007/978-1-4020-4333-8_12
21. Vandenbosch GAE, Volski V, Verellen N, Moshchalkov VV (2011) On the use of the method of moments in plasmonic applications. *Radio Sci* 46(05):1–6. <https://doi.org/10.1029/2010RS004582>
22. Archambeault B, Ramahi OM, Brench C (1998) The finite-difference time-domain method," in *EMI/EMC Computational Modeling Handbook*, B. Archambeault, O. M. Ramahi, and C. Brench, eds. (Springer US, 1998), pp. 35–67. <https://doi.org/10.1007/978-1-4757-5124-6>
23. Vandenbosch GAE (2012) Computational Electromagnetics in Plasmonics (IntechOpen, 2012). <https://doi.org/10.5772/51166>
24. Lumerical Inc. "Broadband Fixed Angle Source Technique (BFAST)". <https://optics.ansys.com/hc/en-us/articles/360034902273-Broadband-Fixed-Angle-Source-Technique-BFAST>. Accessed 1 Mar 2023
25. Zhang J, Irannejad M, Yavuz M, Cui B (2015) Gold nanohole array with sub-1 nm roughness by annealing for sensitivity enhancement of extraordinary optical transmission biosensor. *Nanoscale Res Lett* 10(1):238. <https://doi.org/10.1186/s11671-015-0944-x>
26. Fadakar H, Nezhad AZ, Borji A (n.d.) Effect of surface roughness on propagation of surface plasmon polaritons along thin lossy metal films," 6
27. Pelleg J, Zevin LZ, Lungo S, Croitoru N (1991) Reactive-sputter-deposited TiN films on glass substrates. *Thin Solid Films* 197(1):117–128. [https://doi.org/10.1016/0040-6090\(91\)90225-M](https://doi.org/10.1016/0040-6090(91)90225-M)
28. Su H-C, Lin M-Z, Huang T-W, Lee C-H (2004) A comparison between X-ray reflectivity and atomic force microscopy on the characterization of a surface roughness," *Proceedings of SPIE - The International Society for Optical Engineering* 50. <https://doi.org/10.1117/12.539761>
29. Patsalas P, Kalfagiannis N, Kassavetis S (2015) Optical properties and plasmonic performance of titanium nitride. *Materials* 8(6):3128–3154. <https://doi.org/10.3390/ma8063128>
30. Shkondin E, Repän T, Takayama O, Lavrinenko AV (2017) High aspect ratio titanium nitride trench structures as plasmonic biosensor. *Opt Mater Express* OME 7(11):4171–4182. <https://doi.org/10.1364/OME.7.004171>
31. Judek J, Wróbel P, Michałowski PP, Oźga M, Witkowski B, Seweryn A, Struzik M, Jastrzębski C, Zberecki K (2021) Titanium nitride as a plasmonic material from near-ultraviolet to very-long-wavelength infrared range. *Materials* 14(22):7095. <https://doi.org/10.3390/ma14227095>
32. Genet C, Ebbesen TW (2007) Light in tiny holes. *Nature* 445(7123):39–46. <https://doi.org/10.1038/nature05350>
33. Barnes WL, Murray WA, Dintinger J, Devaux E, Ebbesen TW (2004) Surface plasmon polaritons and their role in the enhanced transmission of light through periodic arrays of subwavelength holes in a metal film. *Phys Rev Lett* 92(10):107401. <https://doi.org/10.1103/PhysRevLett.92.107401>
34. Gao H, McMahon JM, Lee MH, Henzie J, Gray SK, Schatz GC, Odom TW (2009) Rayleigh anomaly-surface plasmon polariton resonances in palladium and gold subwavelength hole arrays. *Opt Express* 17(4):2334. <https://doi.org/10.1364/OE.17.002334>
35. Garcia-Vidal FJ, Martin-Moreno L, Ebbesen TW, Kuipers L (2010) Light passing through subwavelength apertures. *Rev Mod Phys* 82(1):729–787. <https://doi.org/10.1038/srep33126>
36. Lee K-L, Chang C-C, You M-L, Pan M-Y, Wei P-K (2016) Enhancing the surface sensitivity of metallic nanostructures using oblique-angle-induced fano resonances. *Sci Rep* 6(1):33126. <https://doi.org/10.1038/srep33126>

37. Zhou W, Odom TW (2011) Tunable subradiant lattice plasmons by out-of-plane dipolar interactions. *Nature Nanotech* 6(7):423–427. <https://doi.org/10.1038/nnano.2011.72>
38. Rodrigo SG, Martín-Moreno L, Nikitin AY, Kats AV, Spevak IS, García-Vidal FJ (2009) Extraordinary optical transmission through hole arrays in optically thin metal films. *Opt Lett* OL 34(1):4–6. <https://doi.org/10.1364/OL.34.000004>
39. Salah HB, Hocini A, Melouki N, Khedrouche D (2021) Design and analysis of near infrared high sensitive metal-insulator-metal plasmonic bio-sensor. *IOP Conf Ser Mater Sci Eng* 1046(1):012003. <https://doi.org/10.1088/1757-899X/1046/1/012003>
40. Tathfif I, Hassan MDF, Rashid KS, Yaseer AA, Sagor RH (2022) A highly sensitive plasmonic refractive index sensor based on concentric triple ring resonator for cancer biomarker and chemical concentration detection. *Opt Commun* 519:128429. <https://doi.org/10.1016/j.optcom.2022.128429>
41. Rashid KS, Tathfif I, Yaseer AA, Hassan MF, Sagor RH (2021) Cog-shaped refractive index sensor embedded with gold nanorods for temperature sensing of multiple analytes. *Opt Express* OE 29(23):37541–37554. <https://doi.org/10.1364/OE.442954>
42. Rashid KS, Hassan MDF, Yaseer AA, Tathfif I, Sagor RH (2021) Gas-sensing and label-free detection of biomaterials employing multiple rings structured plasmonic nanosensor. *Sens Bio-Sens Res* 33:100440 (2021). <https://doi.org/10.1016/j.sbsr.2021.100440>
43. Tathfif I, Rashid KS, Yaseer AA, Sagor RH (2021) Alternative material titanium nitride based refractive index sensor embedded with defects: an emerging solution in sensing arena. *Results Phys* 29:104795. <https://doi.org/10.1016/j.rinp.2021.104795>
44. Kaur V, Singh S (2019) Design of titanium nitride coated PCF-SPR sensor for liquid sensing applications. *Opt Fiber Technol* 48:159–164. <https://doi.org/10.1016/j.yofte.2018.12.015>
45. Fu T, Chen Y, Du C, Yang W, Zhang R, Sun L, Shi D (2020) Numerical investigation of plasmon sensitivity and surface-enhanced Raman scattering enhancement of individual TiN nanosphere multimers. *Nanotechnology* 31(13):135210. <https://doi.org/10.1088/1361-6528/ab61d3>

Publisher's Note Springer Nature remains neutral with regard to jurisdictional claims in published maps and institutional affiliations.